*Journal of Structural Geology*, Vol. 10, No. 3, pp. 263 to 272, 1988
Printed in Great Britain

0191-8141/88 $03.00 + 0.00


# Application of a three-dimensional finite-element method to strain field analyses

DANIEL D. SCHULTZ-ELA*

Department of Geology and Geophysics, University of Minnesota, Minneapolis, MN 55455, U.S.A.

(*Received* 17 *July* 1987; *accepted in revised form* 15 *September* 1987)

**Abstract**—I have programmed a three-dimensional finite-element model to spatially integrate distributed strains. The mathematics is based on Cobbold and Percevault (1983). The method finds the pre-strain configuration of a region by unstraining rectangular prisms into parallelepipeds, then rotating and translating them iteratively to minimize the interelement deviations. A numerical singular-value decomposition calculates the necessary rotations and the final cycle of further strains to make a best fit of the elements. The deviation of elements from holes formed by their nearest neighbors indicates the degree of compatibility of strain measurements.

The program reproduces the rotations required in examples with analytic solutions. Even though only a single horizontal layer of elements is used, the fitting procedure correctly calculates rotations in all three dimensions from the constraints of strain compatibility.

Three-dimensional strains measured in an Archean greenstone belt of northeastern Minnesota were integrated using a layer of nearly equant finite elements. Rotations calculated from the pre-tectonic configuration accord with field observations of fabrics indicating variable amounts of shear. Rotations about horizontal axes are minimal, precluding large vertical shears. An estimate of 40% true horizontal north–south shortening across the belt can be made from the undeformed configuration.

## INTRODUCTION

IT IS rare to be able to measure the complete deformation a rock has undergone. Generally only the distortion (strain) is measurable. Any rigid-body rotations, translations or dilations can only be inferred in special cases where we have more knowledge of the rock's undeformed configuration. Even rarer is a continuous sampling of a deformation field. Usually, strain can be specified only at distributed locations on a single surface, subject to outcrop availability and presence of suitable strain markers. The strain data also contain measurement errors and a variability inherent in complex rock systems which cannot be quantified except in a statistical manner.

Cobbold & Percevault (1983) proposed a finite-element method for integrating spatially distributed strain measurements subject to these constraints. Using this method, a pre-tectonic configuration can be calculated for the rocks, which facilitates differentiation of tectonic models and unraveling structural complexities. The calculated rotations indicate regions which underwent rotational deformations relative to the bulk field. An iterative best-fit procedure gives a measure of the overall compatibility of strains. Departures from perfect compatibility indicate measurement errors, inhomogeneous dilations, or excessively separated datum locations relative to the variation in the strains.

I have implemented Cobbold & Percevault's method on an IBM PC-compatible microcomputer. A single layer of nearly equant orthorhombic parallelepipeds forms the finite-element array. The input data comprise three-dimensional strain measurements for each element. The elements are unstrained, translated and rotated in all three dimensions to achieve a best-fit. This method has the advantage of using all of the available strain data, rather than using projections of ellipsoids onto a single plane for a two-dimensional fitting procedure. Strains can be integrated from any deformed rocks with strain markers, on all scales from outcrop to orogenic belt.

The computational method will be described first, concentrating on my implementation, with clarifications of Cobbold & Percevault (1983). Examples are shown for which the program reproduces rotations which are independently specified by equations in three dimensions. Finally, a natural strain distribution is used to illustrate the program's utility.

## FINITE-ELEMENT METHOD

### *Element co-ordinates*

My strain integration program is based on the theory of Cobbold & Percevault (1983). Consequently their notation is employed where applicable. Deformation is specified by the transformations

$$\mathbf{z} = \mathbf{z}(\mathbf{Z}) \tag{1}$$

and

$$\mathbf{Z} = \mathbf{Z}(\mathbf{z}), \tag{2}$$

*Current address: Department of Geology, Colorado College, Colorado Springs, CO 80903, U.S.A.

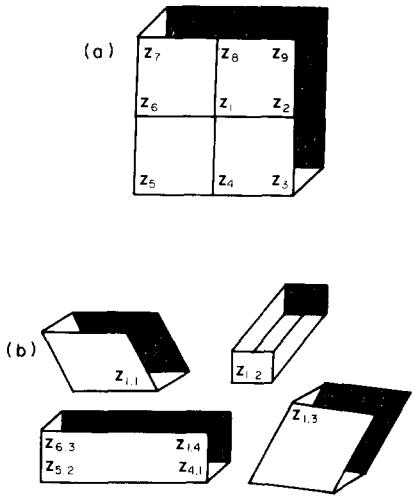


Fig. 1. Numbering system for boundary points **Z**. Elements are viewed from the top in the $+z_3$ direction, the bottom surfaces are patterned. (a) Deformed configuration. The subscript specifies the global index of the point. (b) Undeformed configuration. The second subscript specifies the local corner of the global boundary point.

where **z** and **Z** are the Cartesian vector co-ordinates of a material point in the deformed and undeformed states, respectively. The mathematics presented here is valid for an array of elements in all three dimensions. However, since strain measurements are generally only available on one surface, in the program a single layer of orthorhombic parallelepipeds constitutes the element array in the deformed state. The elements are also parallelepipeds in the undeformed state, with boundary points defined by **Z**.

A global numbering system is established for boundary point co-ordinates **z**, as well as a local system for each element. Boundary points shared between elements in the deformed state no longer coincide in the undeformed state, so another index is needed in the global co-ordinate array to specify the 'corner' of the global boundary point (Fig. 1).

The program finds the undeformed configuration of the elements by calculating a sequence of intermediate states **Y**. The array elements are first unstrained homogeneously, then translated, and finally rotated to optimize the overall fit. (As used here, 'unstrained' refers only to the removal of the distortional component of the deformation.) Each of these steps transforms the element boundary points to a new state.

*Unstraining*

Usually only the distortion of a rock is measurable. The distortion to be removed is specified by the reciprocal of a strain measurement in that element. (Details of how these strains are specified for both simulated and natural examples are included in sections below.) This irrotational strain is assumed to be homogeneous in each element. The state with the distortion removed is intermediate between **z** and **Z**, and is defined by **Y**, the boundary point co-ordinate vectors. For the conditions of a homogeneous, irrotational strain, we have

$$\mathbf{Y} = \mathbf{M}^{-1}\mathbf{z}, \tag{3}$$

where $\mathbf{M}^{-1}$ is a symmetrical 3 × 3 matrix with constant components in the global Cartesian co-ordinate system.

Strain measurements are usually reported as principal strain values and orientations. In the principal-axis co-ordinate system of an element, with measured principal stretches $S_i$, $\mathbf{M}^{-1}$ becomes a diagonal matrix $\mathbf{M}^{-1'}$ with the reciprocals of the $S_i$ on its diagonal. The measured principal axis orientations can then be used to define a direction cosine matrix to transform $\mathbf{M}^{-1'}$ to $\mathbf{M}^{-1}$ in Cartesian co-ordinates. This tensor transformation is valid because $\mathbf{M}^{-1}$ is a particular form of $\mathbf{F}^{-1}$, the deformation gradient tensor.

Strain ellipsoid determination methods such as PASE5 of Roberts & Siddans (1971) calculate up to six solutions. If the principal axis orientations are averaged, the axes may not be quite orthogonal. The axes can be orthogonalized by holding the best constrained axis fixed ($S_1$ = maximum elongation for constrictional strain, $S_3$ for flattening). For $S_1$ fixed, $S_2$ is rotated within the $S_1$–$S_2$ plane until it lies in the plane normal to $S_1$. $S_3$ is found by taking the vector cross-product of $S_1$ and $S_2$, which also ensures the axes form a right-handed system. In practice, the adjustment of the two less well-constrained axes is generally less than 5°. This orthogonalization may be avoided if Owens's (1984) best-fit ellipsoid determination is employed.

*Element-hole deviation*

After the elements are unstrained, the distance between face centers of adjacent elements is minimized. An equivalent process is to minimize the deviation between elements and the hole defined by their nearest neighbor elements. Let **Y*** be the boundary points of the hole. Then the deviation, $\mathfrak{D}$, is defined as

$$\mathfrak{D} = \frac{1}{n}\sum_{1}^{n} |\mathbf{Y}^* - \mathbf{Y}|^2 = \sum_{I=1}^{3} \overline{(Y_I^* - Y_I)^2}, \tag{4}$$

where $n$ is the number of boundary points and the bar indicates an arithmetic mean (Cobbold & Percevault 1983). An element with eight corners occupies a hole defined by four nearest neighbors with 16 boundary points. A new hole with eight boundary points is specified by the vector means of pairs of adjacent boundary points (Fig. 2a). The deviation is the same for both holes, so the new hole is used in the following.

A problem arises when an element lies on an edge or corner of the array. The hole it occupies is incompletely specified. For an edge element with three nearest neighbors, a smaller hole is defined as shown in Fig. 2(b), and only the inside half of the element is used in the fitting procedure. The edge centers of the neighboring edge-elements are the outer boundary points of the hole. For a corner element with two nearest neighbors, only the inner quarter of the element is used for fitting. Six of the hole's boundary points are formed by the edge centers and inner corner means (Fig. 2c). The remaining two outer corners are projections outward such that the

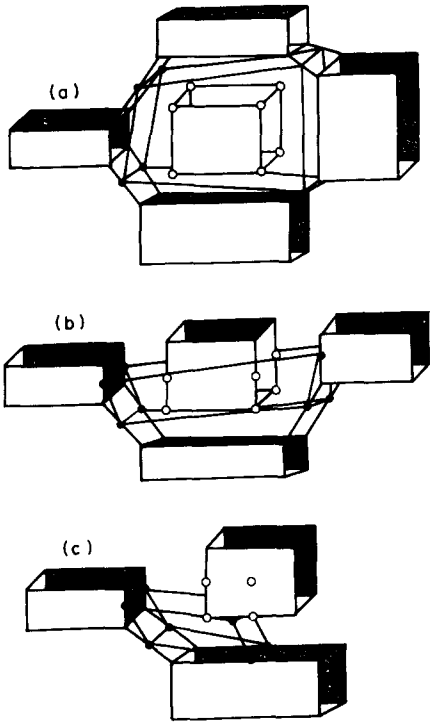


Fig. 2. Construction of element holes. Thin solid lines connect corners of nearest neighbor elements defining the hole. Solid circles are corners of hole (see text for definition). Open circles are corners of element portion to be fitted in the hole. Dotted lines bound the hole. (a) Element with four nearest neighbors. (b) Element on an edge of the array with only three nearest neighbors. (c) Element on a corner of the array with only two nearest neighbors.

planes bounding the top and bottom of the hole are parallelograms.

The procedure for fitting elements into their holes is analogous to the modified Euler method for approximating curves by line segments (Cobbold & Percevault 1983). Here, by minimizing the distances between face centers of elements, I essentially start with the line segments through the element centroids, then fit them together end-to-end. By defining edge and corner holes as above, the centroid of the element to be fitted is analogous to the endpoint of the modified Euler curve. The segment is only projected inward from the centroid. When the deviation, $\mathfrak{D}$, is minimized, the face center distances will also be minimized.

*Translations*

As Cobbold & Percevault (1983) have shown, rigidly translating the element in its hole until their vector means coincide minimizes $\mathfrak{D}$ with respect to translations. For the state **Y** (distortion removed), the translation vector, **B**, is given by

$$B_I = \overline{Y_I^*} - \overline{Y_I}. \tag{5}$$

Adding **B** to the element boundary points yields a *new* intermediate state **Y**, where $\overline{Y_I^*} = \overline{Y_I}$.

*Rotations*

Rigidly rotating the element about its centroid does not affect the previous minimization step. To solve for the unknown rotations, we first need to define

$${}_oY_I = Y_I - \overline{Y_I}, \tag{6}$$

where the $_o$ subscript symbolizes the deviation of a component from the mean value and the $Y$ components are for the intermediate state following translation **B**. For a rotation tensor, $R_{IJ}$, rotation of a rigid element in a stationary hole is expressed by

$${}_oZ_I^* = {}_oY_I^*, \tag{7}$$

and

$${}_oZ_I = R_{IJ}\,{}_oY_J$$

(Cobbold & Percevault 1983, equation 14). If (4) is regarded as the deviation in the final state, with $Y$ variables replaced by $Z$, then substituting (7) into (4) yields

$$\mathfrak{D} = \sum_{I=1}^{3} \overline{({}_oY_I^*)^2} + \sum_{I}^{3} \overline{({}_oY_I)^2} - 2 \sum_{I}^{3} \sum_{J}^{3} R_{IJ}\,\overline{{}_oY_I^*\,{}_oY_J} \tag{8}$$

(Cobbold & Percevault 1983, equation 15).

Only the last term of (8) is affected by rotation. In terms of matrices, $R_{IJ}\,\overline{{}_oY_I^*\,{}_oY_J}$ can be viewed as a scalar product, $\mathbf{R}:\mathbf{Y}'$, where **R** is the matrix of components $R_{IJ}$ and $\mathbf{Y}'$ is the matrix of components $\overline{{}_oY_I^*\,{}_oY_J}$. From Malvern (1969, equation 2.4.25b), scalar products behave as

$$\mathbf{R}:\mathbf{Y}' = \mathrm{tr}(\mathbf{R}^{\mathrm{T}}\cdot\mathbf{Y}'), \tag{9}$$

where the right-hand term is the trace of the tensor product of **R**-transpose and $\mathbf{Y}'$. To minimize **D**, $\mathbf{R}\cdot\mathbf{Y}'$ must be maximized because the first two terms of (8) are invariant with respect to rotation. The trace of a tensor is maximum if the tensor is symmetric (Cobbold & Percevault 1983) so we need to find **R** such that $\mathbf{R}^{\mathrm{T}}\cdot\mathbf{Y}'$ is symmetric. $\mathbf{Y}'$ may be decomposed into a product of orthogonal and symmetrical matrices **O** and **S**, that is

$$\mathbf{Y}' = \mathbf{O}\cdot\mathbf{S}. \tag{10}$$

Therefore, to make $\mathbf{R}\cdot\mathbf{Y}'$ symmetric and maximum, **R** needs to satisfy

$$\mathbf{R}^{\mathrm{T}}\cdot\mathbf{O} = \mathbf{I}, \tag{11}$$

where **I** is the unit tensor. **R** is orthogonal, so from (11),

$$\mathbf{R} = \mathbf{O}. \tag{12}$$

Determination of the rotation matrix now reduces to finding **O** in the decomposition of (10). A singular value decomposition (SVD) for general symmetric matrices (Nash 1979) can be used to find **O**, and will be shown to be useful in other applications below. Decomposing $\mathbf{Y}'$ with the SVD gives

$$\mathbf{Y}' = \mathbf{U}\cdot\mathbf{S}\cdot\mathbf{V}^{\mathrm{T}}. \tag{13}$$

**U** and **V** are orthogonal matrices, and **S** is a diagonal matrix composed of the singular values of $\mathbf{Y}'$. The columns of **U** and **V**, respectively, are the left and right singular vectors of $\mathbf{Y}'$. **O** rotates the columns of **V** into those of **U** (Malvern 1969, pp. 176–177, DePaor 1983, equation 79).

In (7) the $Y_I$ are known, the $Z_J$ are to be calculated, so using (12), the overall goal is to find **O**, where

$$_oZ_J = O_{IJ}\ _oY_I. \tag{14}$$

Using equation (4.6.11) of Malvern (1969) with column vectors and the SVD in (13), the rotations which minimize the deviations are

$$O_{IJ} = V_{IK}U_{JK}. \tag{15}$$

Rotations and translations are performed for each element sequentially. Their holes include elements already fitted. After the entire array is fitted, the process is initiated again, continuing iteratively until the sum of adjustments in the last cycle is negligible. A total rotation matrix for each element can be saved by left-multiplying the cumulative rotation by the rotation matrix at each step.

To speed the process, a 'fast-packing' step precedes the iterative-packing, as suggested by Cobbold & Percevault (1983). The hole for an element is only specified by the inner nucleus of elements already packed. For an element on the edge of the nucleus, a hole is projected outward from the single packed element it borders. Because the position of the outer face of the hole is not constrained, after the element is fitted in the hole it is translated again until its inner face center adjoins that of the packed element. Corner elements are done last, and their holes are projected outward from the two packed elements they border (Fig. 2c).

The program uses arrays comprising both the packing order of the elements and their outward-facing directions during both the fast-pack and iterative-pack cycles. The facing directions tell the program which neighboring elements are to be used to define the hole.

Convergence is measured by both the sum of element-hole deviations and the change in that sum from the preceding packing cycle. The program halts when the change falls below some preset tolerance. The sum of the deviations correlates with the compatibility of the elements. Unfortunately, it is difficult to quantify that relation. The deviation sum need not be zero for a complex strain field, even if the strains are perfectly compatible. This departure reflects the approximations inherent in the underlying numerical methods. As noted by Cobbold & Percevault (1983), the deviation sum will be zero for strain fields described by polynomial coordinate transformations of order 2 or less (see examples below).

*Further strain and rotation*

After the translation and rotation steps, the elements can be strained further for a better fit. Large strains so determined indicate a lack of compatibility in the measured strains, which could be due to measurement errors, an excessively coarse element grid relative to changes in the strain field, discontinuities in the strain field, or unknown heterogeneous dilations across the field. Differential dilations during the deformation will be indicated by differential dilations of the opposite sense during the further strain step.

If we begin with an intermediate state after the preceding fitting routine, the general deformation of the elements is described by

$$_oZ_I^* = {}_oY_I^*,$$
$$_oZ_I = D_{IJ}\ _oY_J \tag{16}$$

(Cobbold & Percevault 1983, equation 16).

Substituting (16) into (4) (with $Z$ variables in (4) describing the final state) and minimizing yields

$$D_{IK}\overline{(_oY_K\ _oY_J)} = \overline{_oY_I^*\ _oY_J}. \tag{17}$$

Equation (17) is summed on $K$ only to form nine equations for the nine unknown $D_{IK}$.

Let **Y′** be the matrix composed of $\overline{_oY_K\ _oY_J}$. The SVD is used to invert **Y′**. If

$$\mathbf{Y'} = \mathbf{U}\cdot\mathbf{S}\cdot\mathbf{V}^{\mathrm{T}}, \tag{18}$$

then

$$\mathbf{Y'}^{-1} = \mathbf{V}\cdot\mathbf{S}^{-1}\cdot\mathbf{U}^{\mathrm{T}} \tag{19}$$

(Nash 1979). Because **S** is diagonal, calculation of (19) is straightforward through

$$S_{ii}^{-1} = 1/S_{ii}, \tag{20}$$

and the orthogonality of **U** and **V**. Then

$$D_{IK} = \overline{(_oY_I^*\ _oY_J)}\,\overline{(_oY_J\ _oY_K)}^{-1}. \tag{21}$$

If the elements are only allowed to dilate, with $\lambda$ the dilation, then

$$\lambda = \sum_I^3 \overline{(_oY_I^*\ _oY_I)} \Big/ \sum_I^3 \overline{(_oY_I)^2} \tag{22}$$

(Cobbold & Percevault 1983, equation 20).

The principal values and orientations of the further strains are calculated with the SVD. If $\mathfrak{D}$ is the further strain matrix, then

$$\mathbf{D} = \mathbf{U}\cdot\mathbf{S}\cdot\mathbf{V}^{\mathrm{T}} \tag{23}$$

**S** has the principal values on its diagonal, the columns of **U** are the vector orientations of the corresponding principal axes in the deformed state, and the columns of **V** are the principal axis orientations in the undeformed state (Shore & Duncan 1984). The rotation component, **R**, of the deformation is

$$R_{IJ} = U_{IK}V_{JK} \tag{24}$$

(Malvern 1969, equation 4.6.11 modified for column vectors; DePaor 1983, equation 79 in component form).

During the further strain-fitting, all of the elements are fitted into the holes calculated by the iterative packing routine, rather than sequentially fitting an element, then defining a new hole based on it for the next element. In this way, the further strains are insensitive to the fitting order. Because iteratively packed holes are defined by the mean of boundary points of adjacent elements, further strains calculated with them ensures that the elements approach each other with minimum gaps or overlaps.

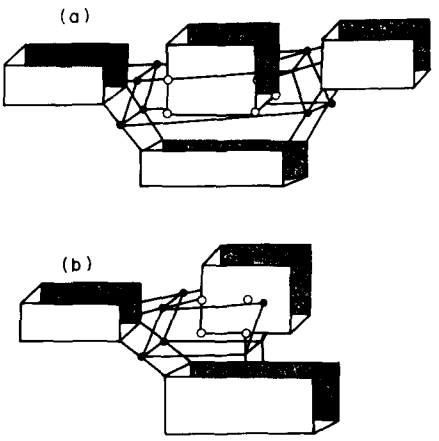


Fig. 3. Construction of holes for further strain step. Symbols as in Fig. 2. (a) Element on an edge of the array with only three nearest neighbors. (b) Element on a corner of the array with only two nearest neighbors.

Holes for edge and corner elements need to be defined differently for the further strain calculations. If a hole is specified as in Fig. 2(b) or (c), the outer boundary points of the hole lie on the adjacent elements. An element further strained to fit this hole will overlap the adjacent element when it too is further strained in the hole defined by the first element.

To make the face centers of edge and corner elements coincide after further strains, their holes are specified as shown in Fig. 3. The holes' outer boundary points are the means of midpoints of the adjacent edges of the fixed element and the element to be strained. This procedure can be criticized on the grounds that the element to be strained partially determines its hole, but in the absence of further information, this seems to be the best approach.

## EXAMPLES WITH ANALYTICAL SOLUTIONS

Transformation equations such as (1) and (2) can be used to describe a strain field. To test whether the program reproduces the rotations calculable from the equations, they were solved for finite strains for the co-ordinates of the element centroids in the deformed state. These data formed the program input. The computer then calculated the rotations and translations, which indeed matched those found by solving the equations.

### *Examples*

Figure 4 shows the initial finite-element array comprising a single layer of 48 cubes. This array represents the *deformed* state. The succeeding figures all show the *undeformed* state. In Figs. 4–11 the arrays are viewed from above in a perspective projection with the viewpoint distance approximately 4 times the maximum dimension of the plot. Thus, parallel element boundaries appear to converge downward (i.e. in the $+z_3$ direction). The top planes of the elements are outlined with bold

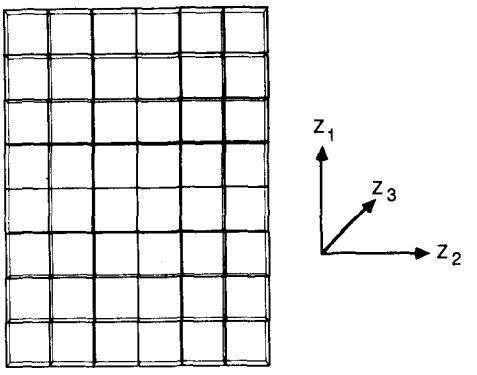


Fig. 4. Initial finite-element array of 48 cubes viewed in perspective in the $+z_3$ direction. Top surfaces of the elements are outlined in bold. This array represents the *deformed* state.

lines. In figures showing horizontal ($z_1$ or $z_2$) views, the viewpoint is located relative to the middle of the row or column displayed, and the bottom surfaces of the elements are hatched. A mainframe computer generated the element plots using a three-dimensional graphics program.

The plots resulting from the fast-packing step are shown with rotations suppressed. Rotations calculated by the program are shown diagrammatically by comparing these plots with those following the iterative-packing cycles.

For the artificial strains, an isochoric deformation is specified with equations (2). The Cartesian co-ordinate axes $z_1$, $z_2$ and $z_3$ are oriented north, east and down (into the page), respectively. The reciprocal deformation gradient tensor $\mathbf{F}^{-1}$ is given by

$$F_{Ij}^{-1} = \partial Z_I/\partial z_j \quad (Ij = 1, 2, 3). \tag{25}$$

The principal values and orientations of the strain can be found from $\mathbf{F}^{-1}$ for the co-ordinates of each element's centroid with the SVD. These data constitute the program's input.

Figure 5 shows the results for a one-dimensional inhomogeneous simple shear (plane strain), with maximum shear strain $\gamma = 2$ at the center of the field. For this deformation, the reverse deformation transformation, (2), is

$$\begin{aligned} Z_1 &= z_1, \\ Z_2 &= 0.04167z_1^3 - 2z_1 + z_2, \\ Z_3 &= z_3 \end{aligned} \tag{26}$$

and the reciprocal deformation gradient tensor is

$$\mathbf{F}^{-1} = \begin{bmatrix} 1 & 0 & 0 \\ 0.125z_1^2 - 2 & 1 & 0 \\ 0 & 0 & 1 \end{bmatrix}. \tag{27}$$

This deformation is analogous to a shear zone with no deformation in the wall rocks. For this relatively simple example, the elements fit together perfectly in the undeformed state after iterative packing (Fig. 5b).

Figure 6 shows the results for two-dimensional inhomogeneous simple shear with the shear in the negative $z_3$-direction (normal to the plane of the elements).

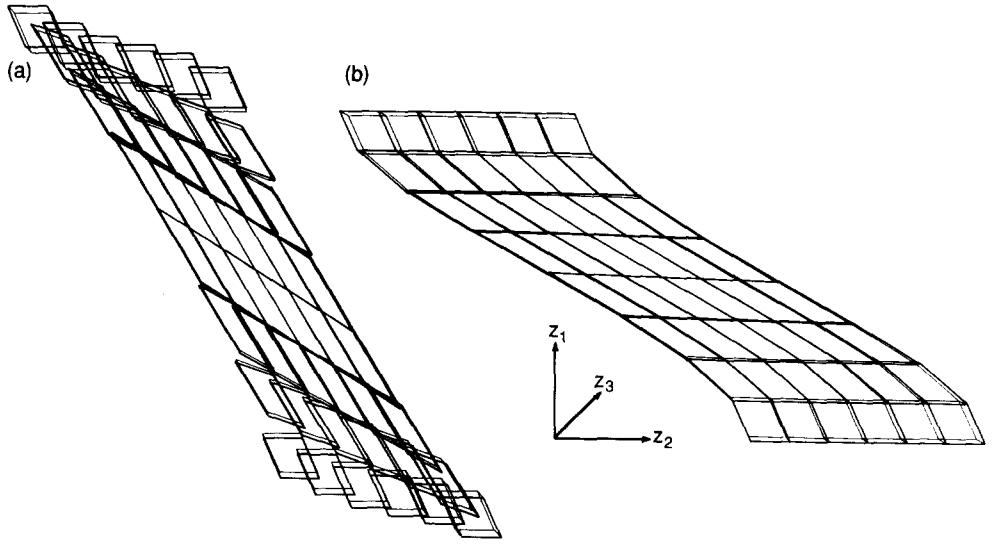


Fig. 5. Results for simple shear in one-dimension ($z_2$-direction), representing a plane strain shear zone (equation 26). Shear increases from $\gamma = 0$ at the zone boundaries to $\gamma_{max} = 2$ at the center. Diagrams are for the *undeformed* state. (a) Configuration of elements after unstraining and translations ('fast-packing' with no rotations). (b) Elements after iterative-packing. Rotation of elements is illustrated by comparing (a) with (b).

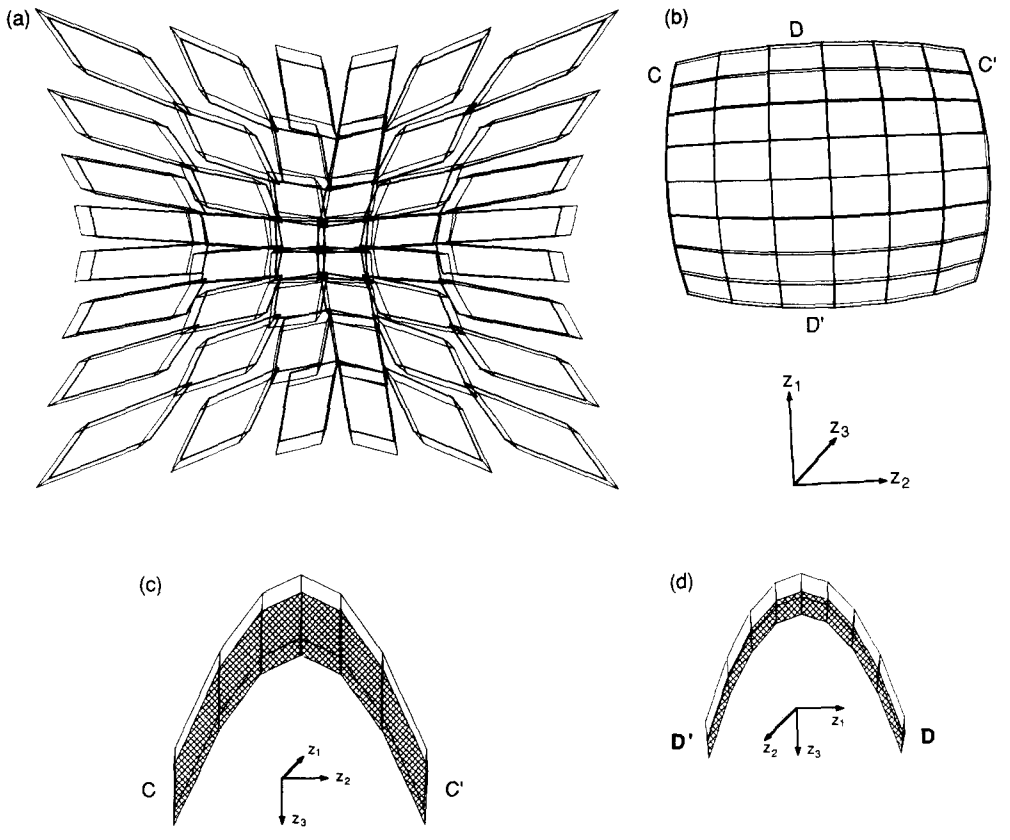


Fig. 6. Results for shear in the vertical ($z_3$) direction with a superimposed pure shear parallel to the co-ordinate axes (equation 28). (a) Elements after fast-packing with no rotations. Axes as in (b). (b) Elements after iterative packing. (c) View in the $+z_1$ direction showing the element row marked C–C'. (d) View in the $-z_2$ direction showing the element column D–D'. In (c) and (d) the elements are hatched on the surfaces facing the viewer which correspond to the lower ($+z_3$) surface in (b).

In addition, a pure shear has been superimposed. The reverse deformation transformations are

$$\begin{aligned} Z_1 &= z_1, \\ Z_2 &= 1.5z_2, \\ Z_3 &= 0.33z_1^2 + 1.69z_2^2 + 0.67z_3 \end{aligned} \tag{28}$$

and the reciprocal deformation gradient tensor is

$$\mathbf{F}^{-1} = \begin{bmatrix} 1 & 0 & 0 \\ 0 & 1.5 & 0 \\ 0.67z_1 & 3.375z_2 & 0.67 \end{bmatrix}. \tag{29}$$

The deformation in (29) can be viewed as separate events of shear and shortening, as in Coward & Potts (1983). The forward pure shear (plane strain) has a stretch of 0.67 in the $z_2$-direction and a stretch of 1.5 in the $z_3$-direction. For shear preceding shortening, (29) corresponds to a forward deformation with shear strains of $\gamma_{z_3z_1} = -0.67z_1$ and $\gamma_{z_3z_2} = -z_2$ for shear in the $z_1z_3$ and $z_2z_3$ planes, respectively. For the case of shortening preceding shear, the shear strains are $\gamma_{z_3z_1} = -z_1$ and $\gamma_{z_3z_2} = -2.25z_2$.

Figure 6(a) shows the elements after fast-packing, with all of the elements still in the $z_1z_2$ plane. The elements converge to a perfect fit in Fig. 6(b). The outer elements in this figure appear smaller because these elements have moved in the positive $z_3$-direction to form a domed surface on the perspective projection. Figures 6(c) & (d) are horizontal views through the array. Even though there is only one layer in the array, the strain compatibility requirements allow the program to correctly compute the necessary rotations in all dimensions, rather than just rotations about vertical axes.

Figure 7 shows the results for a more complex deformation which cannot be described simply in terms of pure or simple shear. The reverse deformation transformations are

$$\begin{aligned} Z_1 &= z_1 - 0.15z_1^2 + 0.2z_1z_2 - 0.67z_2^2, \\ Z_2 &= -0.225z_1^2 + 0.3z_1z_2 + z_2 - 0.1z_2^2, \\ Z_3 &= 0.1z_1^2 + 0.02z_1^3 + 0.2z_2^2 + z_3 \end{aligned} \tag{30}$$

and the reciprocal deformation gradient tensor is

$$\mathbf{F}^{-1} = \begin{bmatrix} (1 - 0.3z_1 + 0.2z_2) & (0.2z_1 - 0.133z_2) & 0 \\ (-0.45z_1 + 0.3z_2) & (1 + 0.3z_1 - 0.2z_2) & 0 \\ (0.2z_1 + 0.06z_1^2) & 0.4z_2 & 1 \end{bmatrix}. \tag{31}$$

The element edges are not coincident in Fig. 7 because of the cubic term in (30). But the face centers coincide as they should for a good fit. Figures 7(b)–(d) show horizontal views through the undeformed array, again illustrating the proper rotations in all three dimensions.

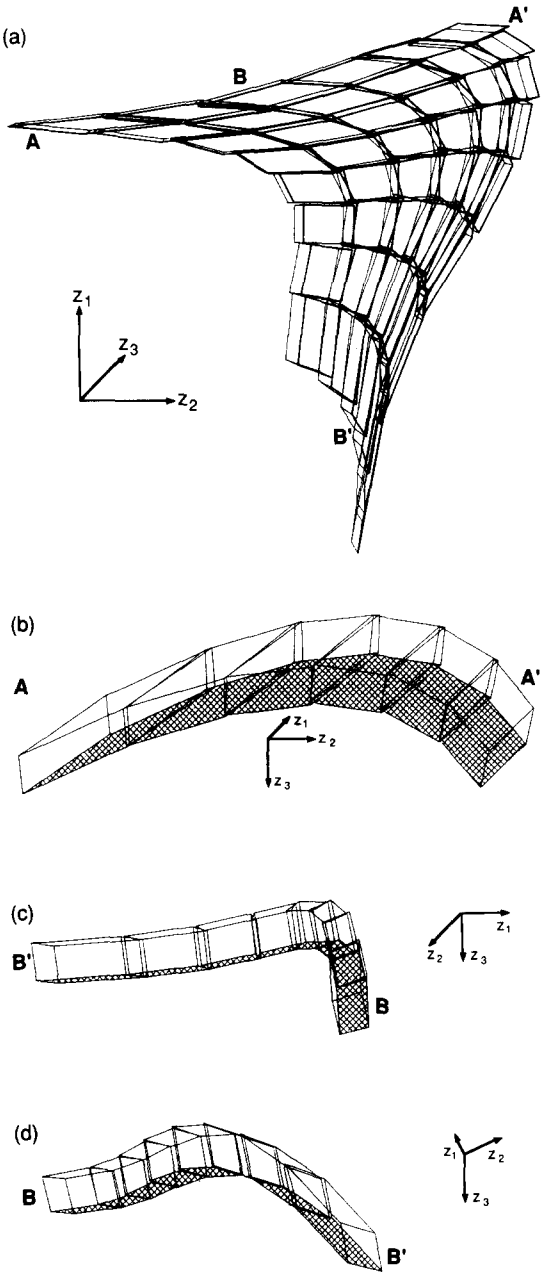


Fig. 7. Results for the deformation in equation (30). (a) Elements after iterative packing. (b) View in the $+z_1$ direction showing the element row marked A–A'. (c) View in the $-z_2$ direction showing the element column B–B'. (d) View directed midway between the $+z_1$ and $+z_2$ axes showing the element column B–B'. In (b) and (c) the elements are hatched on the surfaces facing the viewer which correspond to the lower ($+z_3$) surface in (a). In (d) the bottom hatched surface faces toward the viewer at B and away from the viewer at B'.

## NATURAL EXAMPLE

The Vermilion district of northeastern Minnesota lies in an east–west-trending Archean greenstone belt of low-grade metasedimentary and metavolcanic rocks. Higher-grade granitic rocks occur to the north and south. The late-stage, dextral strike-slip Vermilion fault forms the northern boundary. Fabrics indicate much of the deformation resulted from ductile dextral shear, especially in the northern part of the region where the Vermilion fault is probably the latest, most brittle expression (Hooper & Ojakangas 1971, Sims 1972, 1976, Hudleston 1976, Ela & Hudleston 1985, Hudleston *et al.* 1986).

Competent greenstone and iron-formation cores a major antiformal structure in the east (Fig. 8). Surrounding volcanic metagraywackes and slates show more

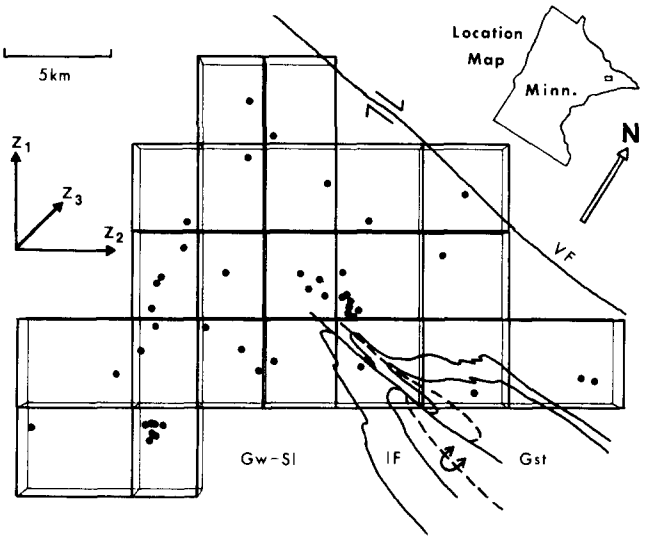


Fig. 8. Initial array of 21 elements for the Vermilion district (representing the present, deformed state). Dots represent sample locations where a strain measurement was made. General geologic contacts shown, with rock units: Gw–Si—metagraywackes and slates; IF—interbedded iron formation and mafic metavolcanics; Gst—mafic metavolcanics, dominantly pillow basalts. The Vermilion Fault is labelled VF.

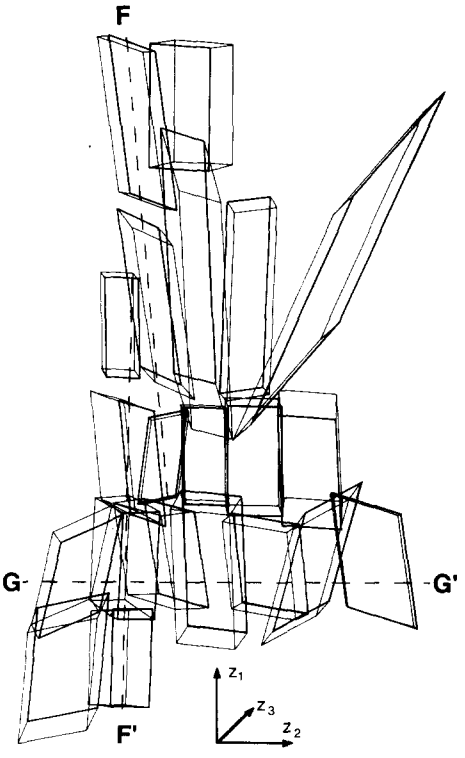


Fig. 9. Array of Fig. 8 after unstraining and fast-packing with no rotations. Dashed lines F–F′ and G–G′ mark element columns and rows shown as horizontal views in Fig. 10(b) & (c).

intensive folding and strain fabrics. Measured strains vary across generally parallel, ENE-trending bands. The largest measured strains are consistently near the Vermilion fault, and they are predominantly of flattening symmetry. Constrictional strains occur to the south, with a mixed zone in between. Maximum shortening ($\lambda_3$) directions plunge shallowly north or south. Maximum elongations plunge 30–60°E for constrictional samples, but plunge more steeply east or west in the flattening zone (Ela & Hudleston 1985).

Relief in the Vermilion district is negligible relative to the areal dimension, allowing a planar approximation of the glaciated ground surface. A full three-dimensional array of elements could be used in other areas where the relief exposes a sufficient number of horizontally *and* vertically distributed sample localities. The method discussed above can be easily extended to such an array.

Forty-seven strain measurements have been made in rocks at 45 distributed locations across the Vermilion district (Fig. 8). A division of the area into 21 nearly equant orthorhombic elements represents the *deformed* state. This configuration of elements was chosen to maximize the number of elements, each of which contains at least one strain measurement. In elements containing multiple measurements, the strains were matrix averaged. The measured (or averaged) strain represents the strain in the entire element. The program converges faster and more reliably for approximately equant elements, further constraining the choice of element shapes. Due to limited outcrop, more evenly and closely spaced sample localities were not accessible. Therefore a systematic investigation of the influence of element shape and size on the undeformed configuration could not be attempted. Most of the strain data derive from similar rock types. Strain measurements used as input did not vary consistently with lithology. More detailed information about the strain measurements and their interpretation will be presented elsewhere.

Figure 9 shows the array after unstraining and fast-packing (with only translations allowed). Elements in the top two rows are elongate, correlating with the measured flattening strains. Conversely, the bottom-left elements are shorter, reflecting constrictional strains. The elements are arranged in straight columns, consistent with dominant N–S shortening and a subhorizontal $\lambda_3$ orientation.

Figure 10 displays the elements after iterative packing. Elements 17, 10 and 13 have rotated anticlockwise about vertical axes in Fig. 10(a) when compared to Fig. 9. These elements lie near the present Vermilion fault. Their rotation presumably reflects the northward-increasing dextral shear evidenced in the rock fabrics. The aspect ratios of elements 16, 9 and 2 show the progressive increase in measured flattening strains to the north. Elements 3 and 11 rotated sinistrally when compared with Fig. 9. This rotation may correlate with the general dextral shearing along the northern boundary of the region, or with rotation around the relatively rigid core of greenstone to the southeast concomitant with the N–S shortening deformation. The elements on the left side of Fig. 10(a) have strained with relatively little rotation.

The horizontal views of Fig. 10(b) & (c) indicate that the array was relatively planar in the pretectonic configuration. No large local rotations are observed about horizontal axes, as would be the case for shear off the flanks of a rising diapir. Isoclinal folding of the bedding is pervasive, so there is no way to infer the original

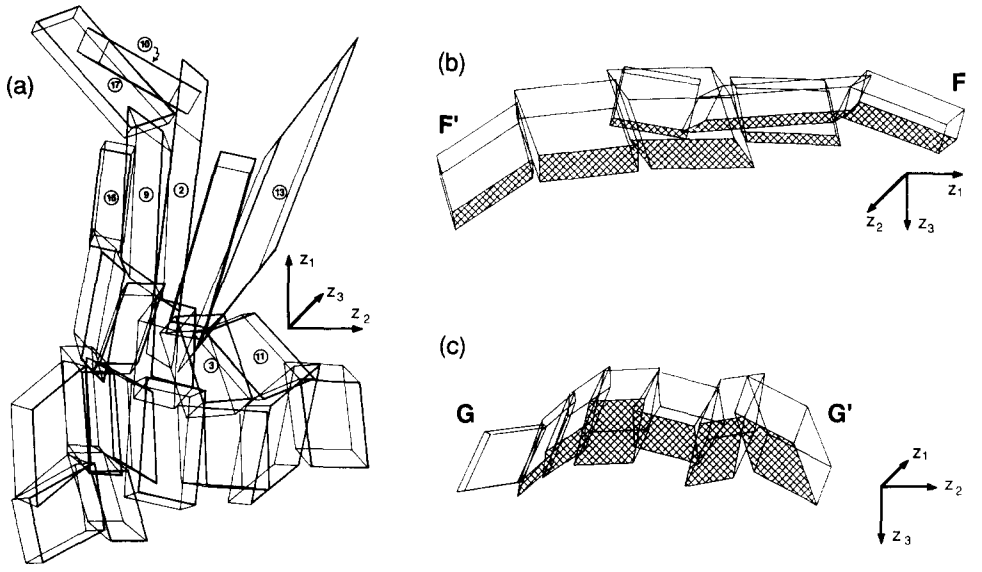


Fig. 10. Array of Fig. 9 after iterative packing. Numbered elements are referred to in the text. (a) View in the $+z_3$ direction. (b) View in the $-z_2$ direction showing elements along line F–F′ in Fig. 9. (c) View in the $+z_1$ direction showing elements along line G–G′ in Fig. 9.

orientation of an entire element in space. Therefore, the bulk rotation of the array during deformation is indeterminate. However, large rotations about a horizontal axis of a rock body that is some 25 km across *after* shortening are unlikely, so a reasonable, if not exact, measure of horizontal shortening can be found by comparing the N–S dimension of the arrays (measured between element centroids) in Figs. 8 and 10(a). A shortening value of 40% is indicated, assuming no volume change.

Figure 11 shows the undeformed configuration after further straining with dilations only allowed. Individual dilations in the top three rows of elements appear to compensate for deviations in strain compatibility between adjacent element. More strain measurements allowing smaller, more numerous elements would probably improve the fit in this area. Elements composing the lowest complete row show consistently negative dilation values. Because measured strain ratios are normalized to no volume change in the deformed state, negative dilations needed to improve fit in the undeformed state may indicate a volume loss during straining.

Overall the elements show reasonable strain compatibility, especially considering the large size of the elements relative to the samples from which the strains were measured. The largest dilation values in Fig. 11 occur in the outer edge elements, where the holes are poorly constrained, so they are not as significant as those in the central region.

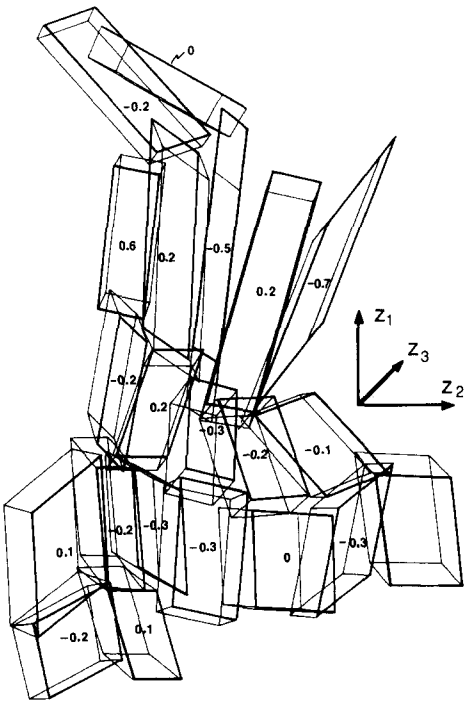


Fig. 11. Elements of Fig. 10 after a further step allowing dilations only to improve element fit. Numbers in elements are dilations relative to elements in Figs. 9 and 10 (0 indicates no dilation).

## CONCLUSIONS

Cobbold & Percevault's (1983) finite-element method for integrating strains has been programmed for a single horizontal layer of three-dimensional elements. A singular-value decomposition efficiently calculates the necessary rotations and further strains. The program reproduces the translations and rotations when they are independently specified by deformation transformation equations. Rotations in all three dimensions are accurately computed from the constraints of strain compatibility. Integration of strains measured at distributed locations in northeastern Minnesota shows the utility of the program for calculating a pretectonic configuration for deformed rocks. The calculated rotations accord with field observations of fabrics indicating variable amounts of subhorizontal dextral shear. Rotations in the vertical direction are minimal. The amount of shortening across the greenstone belt in the (present) N–S, horizontal direction is 40%.

*Acknowledgements*—I am grateful to Peter Hudleston for advice and support on the project, and to the anonymous reviewers for their helpful comments. NSF grants EAR-8206843 and EAR-8408986, and a grant from the University of Minnesota Academic Computing Service provided funds for the research.

## REFERENCES

Cobbold, P. R. & Percevault, M.-N. 1983. Spatial integration of strains using finite elements. *J. Struct. Geol.* **5**, 299–305.

Coward, M. P. & Potts, G. J. 1983. Complex strain patterns developed at the frontal and lateral tips to shear zones and thrust zones. *J. Struct. Geol.* **5**, 383–399.

DePaor, D. G. 1983. Orthographic analysis of geological structures—I. Deformation theory. *J. Struct. Geol.* **5**, 255–277.

Ela, D. & Hudleston, P. 1985. The significance of strain patterns in deciphering the deformational history of Archean rocks in the Vermilion district, Minnesota. *Abs. and Proc., 31st Ann. Mtg.*, Inst. on Lake Superior Geol., 24–25.

Hooper, P. & Ojakangas, R. W. 1971. Multiple deformation in the Vermilion district, Minnesota. *Can. J. Earth Sci.* **8**, 423–434.

Hudleston, P. J. 1976. Early deformational history of Archean rocks in the Vermilion district, northeastern Minnesota. In: *Can. J. Earth Sci.* **13**, 579–592.

Hudleston, P. J., Schultz-Ela, D., Bauer, R. L. & Southwick, D. L. 1986. Transpression as the main deformational event in an Archean greenstone belt, northeastern Minnesota. In *Workshop on Tectonic Evolution of Greenstone Belts* (edited by DeWit, M. J. & Ashwal, L. D.). LPI Technical Rpt. 86–10: 124–126. Lunar and Planetary Institute, Houston.

Malvern, L. E. 1969. *Introduction to the Mechanics of a Continuous Medium*. Prentice-Hall, Englewood Cliffs, New Jersey.

Nash, J. C. 1979. *Compact Numerical Methods for Computers*. John Wiley & Sons, New York.

Owens, W. H. 1984. The calculation of a best-fit ellipsoid from elliptical sections on arbitrarily orientated planes. *J. Struct. Geol.* **6**, 571–578.

Roberts, B. & Siddans, A. W. B. 1971. Fabric studies in the Llwyd Mawr Ignimbrite, Caernarvonshire, North Wales. *Tectonophysics* **12**, 282–306.

Shore, P. J. & Duncan, I. J. 1984. Finite strains from non-coaxial strain paths. I. Computational Techniques. *Tectonophysics* **110**, 127–144.

Sims, P. K. 1972. Vermilion district and adjacent areas. In: *Geology of Minnesota: A Centennial Volume* (edited by Sims, P. K. & Morey, G. B.). Minnesota Geological Survey, St. Paul, Minnesota.

Sims, P. K. 1976. Early Precambrian tectonic–igneous evolution in the Vermilion district, northeastern Minnesota. *Bull. geol. Soc. Am.* **87**, 379–389.